NANO · MICRO small
www.small-journal.com

Interfacial Engineering Enables Perovskite Heteroepitaxial Growth on Black Phosphorus for Flexible X-ray Detectors

Hao Huang, Ying Zheng, Chang Liu, Zhenyu Zhang, Ming Gao, Jiahong Wang, Yanliang Liu, Paul K. Chu, and Xue-Feng Yu**

2D materials with atomic-scale thickness and mechanical robustness are required for flexible devices. The superior optoelectronic properties and high-Z atoms in metal halide perovskites render them desirable for X-ray detection, but the intrinsic brittleness is an obstacle hampering the applications in flexible detectors. Herein, an interfacial engineering strategy is demonstrated for the epitaxial growth of methylammonium lead bromide ($MAPbBr_3$) on black phosphorus (BP) for flexible X-ray detectors. The mechanically robust, high-quality heterostructure consisting of a Pb transition layer is synthesized for the two-way bridging of BP and $MAPbBr_3$. Excellent optoelectronic properties such as a high X-ray sensitivity of 1,609 ± 122 μC Gy^{-1} cm^{-2} (80 times higher than that of the commercial amorphous Se), a fast response time of 40 ± 5 ms, as well as a low detection limit of 3 μGys^{-1} (about a fifteenth of the medical chest X-ray dose rate) are achieved from the simple and planar direct X-ray detector fabricated on an organic filter membrane. More importantly, these flat and simple devices are bendable and mechanically durable by exhibiting only 10% photocurrent degradation after 200 bending cycles. The novel heterostructure has great potential in large-area, flexible, and sensitive X-ray detection applications.

1. Introduction

2D materials have aroused worldwide interest since the discovery of graphene in 2004.[1–3] From organics to inorganics, metals to semiconductors, a myriad of 2D materials have been predicted, discovered, and synthesized,[4–6] for example, polymers,[7] 2D metals,[8] Mxenes,[9] transition metal dichalcogenides[10] and black phosphorus (BP).[11] By taking advantage of the unique 2D nature and physicochemical properties, 2D materials are attractive to electronic devices, energy storage and conversion, optical devices, catalysis, sensors, biomedicine, and so on.[12] More importantly, 2D structures with a large surface area are ideal for different types of heterostructures.[13–15] Also, the atomic-scale thickness and strong in-plane covalent bonds endow them with mechanical robustness and good flexibility boding well for flexible devices.[2,16]

X-ray detectors are crucial to medical imaging, security, and scientific research.[17] Flexible and sensitive X-ray detectors that can convert low-dose X-rays into electronic signals directly can be fitted on nonplanar objects to operate in a tight space.[18–22] Despite the impressive properties of flexible devices designed with rigid X-ray materials and organic semiconductors, there are concerns about possible risks and disadvantages, for example, delamination, large-scale integration, low X-ray absorption efficiency, and the poor charge transport in a finite active layer.[18,19,23] Therefore, it is highly desirable to develop flexible sensitive materials which can absorb X-ray efficiently.

Metal halide perovskites (MHPs) constitute a class of promising active materials for low-cost, high-performance photovoltaic and photodetector applications such as solar cells,[24] light emitting diodes,[25] lasers,[26] and radiation detectors.[27] The superior optoelectronic properties of perovskites including the high defect tolerance, long carrier diffusion lengths, and high light absorption coefficients make them competitive in designing functional heterostructures.[27–29] Moreover, the presence of high-atomic number (Z) elements (e.g., Pb, I) in perovskite MHPs results in strong X-ray absorption for high-sensitivity direct detection of X-rays.[18,30–32] However, the intrinsic brittleness of MHPs hampers application to flexible detectors.[18,33] And furthermore, the grain boundaries in polycrystalline perovskite films are not mechanically robust.[34] Hence, it is challenging to

H. Huang, Y. Zheng, Z. Zhang, M. Gao, Y. Liu, X.-F. Yu
Shenzhen Key Laboratory of Micro/Nano Biosensing
Shenzhen Institute of Advanced Technology
Chinese Academy of Sciences
Shenzhen 518055, P. R. China
E-mail: hao.huang@siat.ac.cn; xf.yu@siat.ac.cn
H. Huang, C. Liu, J. Wang, X.-F. Yu
Hubei Three Gorges Laboratory
Yichang, Hubei 443007, P. R. China
Y. Zheng
Nano Science and Technology Institute
University of Science and Technology of China
Suzhou 215123, P. R. China
P. K. Chu
Department of Physics
Department of Materials Science and Engineering
and Department of Biomedical Engineering
City University of Hong Kong
Tat Chee Avenue, Hong Kong, Kowloon 999077, China

The ORCID identification number(s) for the author(s) of this article can be found under https://doi.org/10.1002/smll.202303229

DOI: 10.1002/smll.202303229

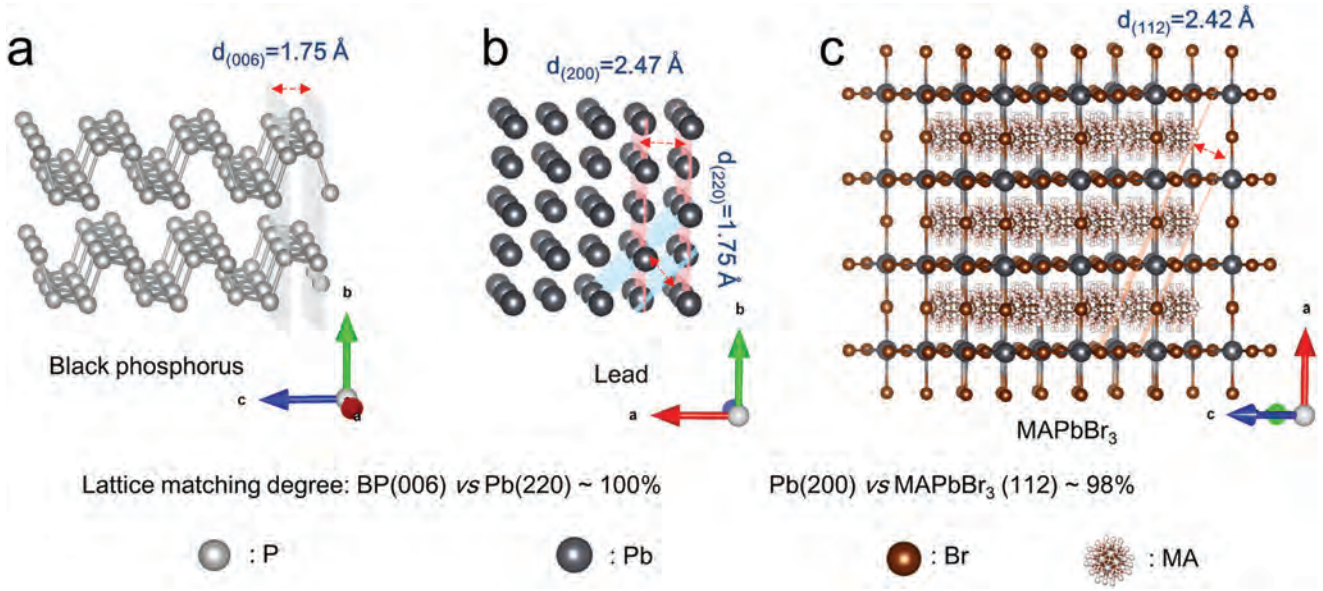

Figure 1. Crystal structure models of BP, lead, and $MAPbBr_3$ and corresponding exposed crystal planes: a) (006) plane of BP, b) (220) and (200) planes of lead, and c) (112) plane of $MAPbBr_3$.

design and fabricate high-performance flexible perovskite-based devices.

BP, a promising class of 2D layered materials with excellent physicochemical properties such as the tuneable bandgap, high carrier mobility, special chemical activity, as well as outstanding mechanical properties,[35–38] has been used to construct heterostructures and flexible devices.[39,40] Herein, an interfacial engineering strategy is demonstrated for the epitaxial growth of methylammonium lead bromide ($MAPbBr_3$) on BP for flexible X-ray detectors. The Pb transition layer is deposited on the BP sheets simultaneously during electrochemical exfoliation. Owing to the lattice match between Pb and BP as well as Pb and $MAPbBr_3$, the Pb transition layer serves as anchor for two-way bridging of BP and $MAPbBr_3$. As a result, the BP-Pb-$MAPbBr_3$ heterostructures are mechanically stronger than the BP-$MAPbBr_3$ heterostructures without the Pb transition layer. To demonstrate the applicaton potentail, a planar direct X-ray detector is fabricated with the BP-Pb-$MAPbBr_3$ heterostructure by simple vacuum filtration. The optoelectronic properties are excellent as manifested by the high X-ray sensitivity of 1609 ± 122 μC Gy^{-1} cm^{-2} (80 times more sensitive than that of conventional α-Se devices) and fast response time of 40 ± 5 ms. Moreover, these simple planar devices exhibiting excellent bending tolerance with only 10% degradation in the photocurrents after 200 bending cycles have enormous potential in flexible X-ray detectors.

2. Results and Discussion

Figure 1 and Figure S1 (Supporting Information) show that the cubic phase lead (Pb) crystal (PDF-04-0686) with the exposed (220) crystal planes has the matching interplanar crystal spacing with the (006) crystal planes of BP (PDF-74-1878) translating into almost 100% lattice matching. Moreover, a relative high lattice match of 98% can be found between the (200) planes of Pb and (112) planes of $MAPbBr_3$ (PDF-00-069-1345). It is believed that good lattice matching facilitates strain-free heteroepitaxial growth on the substrate.[41] Here, a novel heterostructure with Pb serving as the anchoring agent is designed for two-way bridging of BP and $MAPbBr_3$. **Figure 2** illustrates the in situ synthesis of the BP-Pb-$MAPbBr_3$ heterostructures by interfacial engineering of BP. The process includes electrochemical intercalation, activation, deposition, and epitaxial growth. Also, flexible X-ray detectors are fabricated by using such novel heterostructures through a simple vacuum filtration to evaluate the potential application in X-ray detection.

During electrochemical intercalation, tetrabutylammonium bromide (TBAB) is the intercalator, while the bulk BP serves as the cathode and Pt plate as the anode. After initial intercalation, a reverse potential is applied during the addition of HNO_3 to activate the expanded interlayer. The Pb transition layer is then deposited on BP at the same time, followed by further electrochemical exfoliation for 5 min. Figure S2a (Supporting Information) shows that the Raman scattering spectra of the electrochemically exfoliated BP with/without HNO_3 are similar. The X-ray diffraction (XRD) pattern of BP (without activation)-Pb exhibits sharp XRD peaks from BP and cubic-phase Pb. Compared to BP (without activation)-Pb, BP (with activation)-Pb exhibits broad XRD peaks from BP (Figure S2b, Supporting Information), indicating that HNO_3 activation facilitates intercalation and exfoliation of the expanded bulk BP during Pb electrochemical deposition. The XRD spectra acquired at different time (1, 2, 4, and 6 min) confirm deposition of the Pb transition layer on the highly exfoliated BP sheets during the 2-min electrochemical deposition process (Figure S3a, Supporting Information), whereas BP cannot be exfoliated fully in the 1-min process. As expected, the four samples (1, 2, 4, and 6 min) show similar smooth and wrinkled surfaces compared with the directly exfoliated BP sheets (Figure S3b–f, Supporting Information), indicating that the Pb layers are ultrathin and closely integrated with BP.

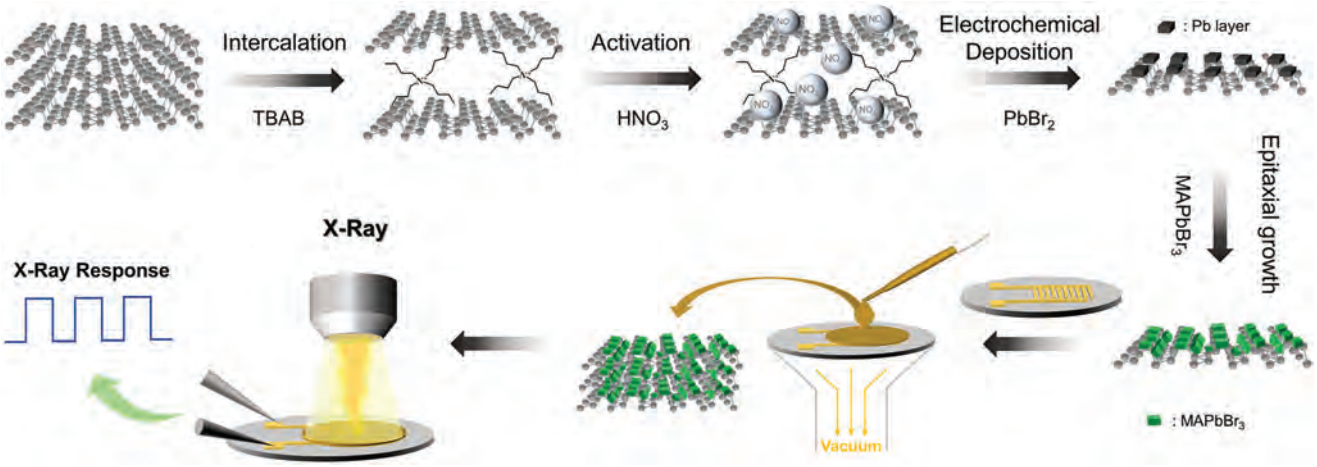

Figure 2. Schematic diagram illustrating the synthesis of the BP-Pb-$MAPbBr_3$ heterostructures and fabrication of the X-ray detector.

Transmission electron microscopy (TEM) and atomic force microscopy (AFM) are performed. As shown in Figure S4a (Supporting Information), the bare BP sheet has a flat and uniform structure and the thickness of the bare BP sheet is determined to be 6 nm based on the vibration of ≈1 nm (Figure S4b, Supporting Information). In comparison, the BP-2 min Pb sheet shows different contrast arising from the BP and Pb layer (dark part) (Figure S4c, Supporting Information). Energy dispersive X-ray spectroscopy (EDS) mapping of the BP-2 min Pb sheet reveals uniformly distributed Pb on the BP surface (Figure S5, Supporting Information) and AFM discloses that BP-2 min Pb has a thickness of 9 nm and larger vibration of ≈1.6 nm (Figure S4d, Supporting Information). These results suggest that the thickness of the Pb layer on the BP-2 min Pb sheet is about 0.6 nm. It is noted that the amount of deposited Pb can be adjusted by altering the electrochemical deposition time, as shown in Figure S6a (Supporting Information) in which a time-dependent increase in the Pb content is revealed and confirmed by XRD Figure S3a (Supporting Information). The high-resolution XPS spectrum of the bare BP shows the typical P 2*p* peak at 129.9 eV and P_xO_y peak at 133.7 eV (Figure S6b, Supporting Information), while higher oxidation resistance is observed after Pb deposition because of the P_xO_y peak diminishes from the 2-min sample. Moreover, all the P 2*p* peaks of the BP-Pb samples shift to lower binding energies indicative of strong interactions between BP and Pb.

In situ epitaxial growth of $MAPbBr_3$ on BP is investigated. As shown in Figure S7a (Supporting Information), the large cubic $MAPbBr_3$ crystals grow on the bare BP sheets. Compared to the bare BP-$MAPbBr_3$, the BP-Pb-$MAPbBr_3$ samples show significant morphological changes (**Figure 3**; Figure S7, Supporting Information) indicating the strong substrate effect rendered by the Pb transition layer and that interfacial engineering of BP plays a vital role in the epitaxial growth of the perovskite heterostructures. As shown in Figure 3a,b the BP-2 min Pb sheets are uniformly decorated with $MAPbBr_3$ nanocrystals with a pyramidal morphology and the average size of 96.4 ± 33.6 nm. The AFM image of the BP-2 min Pb-$MAPbBr_3$ heterostructure is depicted in Figure 3c which shows topographical variation of ≈12 nm and that the $MAPbBr_3$ nanocrystals have a vertical dimension of tens of nanometers. Because the BP is very thin, the TEM image shows a transparent structure of BP-2 min Pb-$MAPbBr_3$ (Figure 3d). The high-resolution TEM (HR-TEM) image of BP-2 min Pb-$MAPbBr_3$ discloses the crystallinity of BP and $MAPbBr_3$ (Figure 3e). The fringe spacings of 4.0 and 2.6 Å are assigned to the (110) plane of $MAPbBr_3$ and (004) plane of BP, respectively.[42] The high-angle annular dark field (HAADF) image in Figure 3f shows a high contrast between the BP-Pb substrate and $MAPbBr_3$ crystals, which is constant with the presence of abundant Pb in $MAPbBr_3$. The chemical composition of BP-2 min Pb-$MAPbBr_3$ is determined by EDS and Figure 3g; Figure S8 (Supporting Information) present the spatial distributions of P, Pb, Br, N, and C.

The sharp XRD peaks in Figure S9a (Supporting Information) confirm the high crystallinity of the $MAPbBr_3$ nanocrystals in the BP-2 min Pb-$MAPbBr_3$ heterostructure. The Raman spectrum of BP-2 min Pb-$MAPbBr_3$ shows the typical Raman peaks of BP as well as those of $MAPbBr_3$ at 322, 967, 1476, and 2967 cm^{-1} compared to the BP-2 min Pb sheets (Figure S9b, Supporting Information).[43] The BP-2 min Pb sheets show a continuous absorption spectrum with no extra signature peaks (Figure S9c, Supporting Information). The small absorption peak at ≈538 nm stems from $MAPbBr_3$ in the BP-2 min Pb-$MAPbBr_3$ heterostructure. The bandgap of $MAPbBr_3$ on BP is calculated to be 2.30 eV. The photoluminescence (PL) spectrum reveals a narrow PL peak with a full-width at half-maximum (FWHM) of 28 nm near the bandgap and indicates a low trapping density in BP-2 min Pb-$MAPbBr_3$.[44] Since the Pb transition layer offers two-way bridging, high-quality $MAPbBr_3$ nanocrystals can be grown epitaxially in situ on BP. As shown in Figure S10 (Supporting Information), the $MAPbBr_3$ crystals in the BP-$MAPbBr_3$ heterostructures synthesized without the Pb transition layer delaminate easily after washing, whereas the BP-2 min Pb-$MAPbBr_3$ heterostructures adhere strongly without peeling off, thus confirming the mechanical stability boding well for flexible applications.

X-ray detectors composed of the BP-Pb-$MAPbBr_3$ heterostructures are prepared by a vacuum filtration method on organic filter membranes (thickness of 100 µm) with pre-fabricated interdigitated gold electrodes (300 µm Au fingers with 100 µm spacing and an effective area of each photodetector of 0.0027 cm^{-2}). **Figure 4**a presents the schematic of the BP-Pb-$MAPbBr_3$-based X-ray

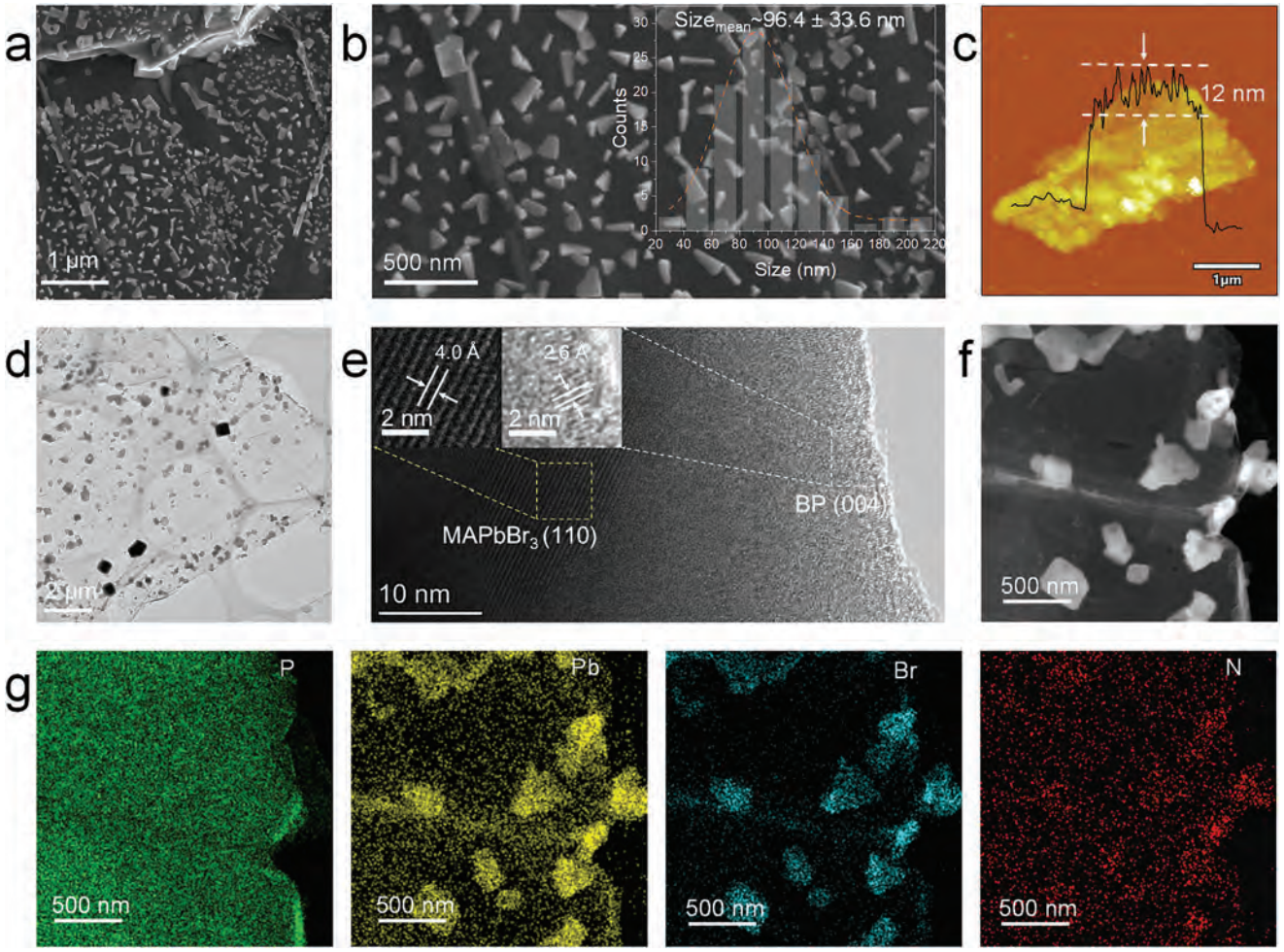

Figure 3. a,b) SEM images of the BP-2 min Pb-MAPbBr$_3$ heterostructure with inset of size distribution of MAPbBr$_3$ crystals (analysis of more than 100 particles), c) AFM image, d–f) TEM, HR-TEM, and HAADF images, and g) EDS maps of BP-2 min Pb-MAPbBr$_3$.

detector. Figure 4b depicts the cross-section of the BP-Pb-MAPbBr$_3$-based film with a thickness of 50 μm and the magnified surface morphology shows a compact structure composed of the layered BP-Pb-MAPbBr$_3$ heterostructure. The X-ray response of the detectors with the BP-MAPbBr$_3$ and BP-Pb-MAPbBr$_3$ heterostructures is evaluated. As shown in Figure 4c, the BP-MAPbBr$_3$ detector shows a photocurrent ($I_{photocurrent} = I_{on}$-$I_{off}$, where I_{on} is the current under X-ray radiation and I_{off} is the dark current) of 1.0 nA at a bias of 10 V bias for a 1.62 mGys^{-1} dose rate. All the BP-Pb-MAPbBr$_3$-based detectors exhibit larger photocurrents, especially BP-2 min Pb-MAPbBr$_3$ showing a photocurrent of 1.7 nA verifying the role of the Pb transition layer in the epitaxial growth of MAPbBr$_3$ and better photoinduced charge separation. P element has a small atomic number and no X-ray response can be observed (Figure S11, Supporting Information), whereas MAPbBr$_3$ is mainly responsible for the X-ray induced photocurrents. To further confirm the effective charge separation and transportation, the BP-2 min Pb-MAPbBr$_3$-based detector is analyzed under exposure of different density 365 nm UV irradiation at a bias of 10 V. As shown in Figure S12 (Supporting Information), the device shows a photocurrent response even at a small power density of 50 μW cm^{-2} and the photocurrents depend of the power densities, thereby revealing that the photoinduced charges are efficiently separated and transported in the BP-Pb-MAPbBr$_3$ and BP-Pb-MAPbBr$_3$ films.

The X-ray detection ability of the BP-2 min Pb-MAPbBr3 detector is assessed systemically. Figure 4d presents the current-voltage (I–V) curves of the device for different X-ray dose rates at biases from −10 to 10 V. A symmetric nonlinear dependence can be observed from the I–V curves as the applied bias increased and that is probably due to the trap-filled process. Higher X-ray induced currents are observed for X-ray dose rates from 0.15 to 1.62 mGys^{-1}. Figure 4e presents the currents of the device for the 1.62 mGys^{-1} X-ray dose rate at biases of 3, 5, 7, and 10 V, and the baseline changes nonlinearly with bias is attributed to the ohmic/Schottky contacts. The currents rise with bias voltages due to promoted charge separation by the electrical field. To further determine the sensitivity of the BP-2 min Pb-MAPbBr3 detector, more than 6 detectors are tested and the photocurrents are monitored for different X-ray dose rates from 32 μGys^{-1} to 1.62 mGys^{-1} (Figure 4f; Figure S13, Supporting Information), all the tested devices have an uncertainty of photocurrent below 8%. The average photocurrents exhibit a saturation trend at the high X-ray dose rates because the limited amount of perovskite

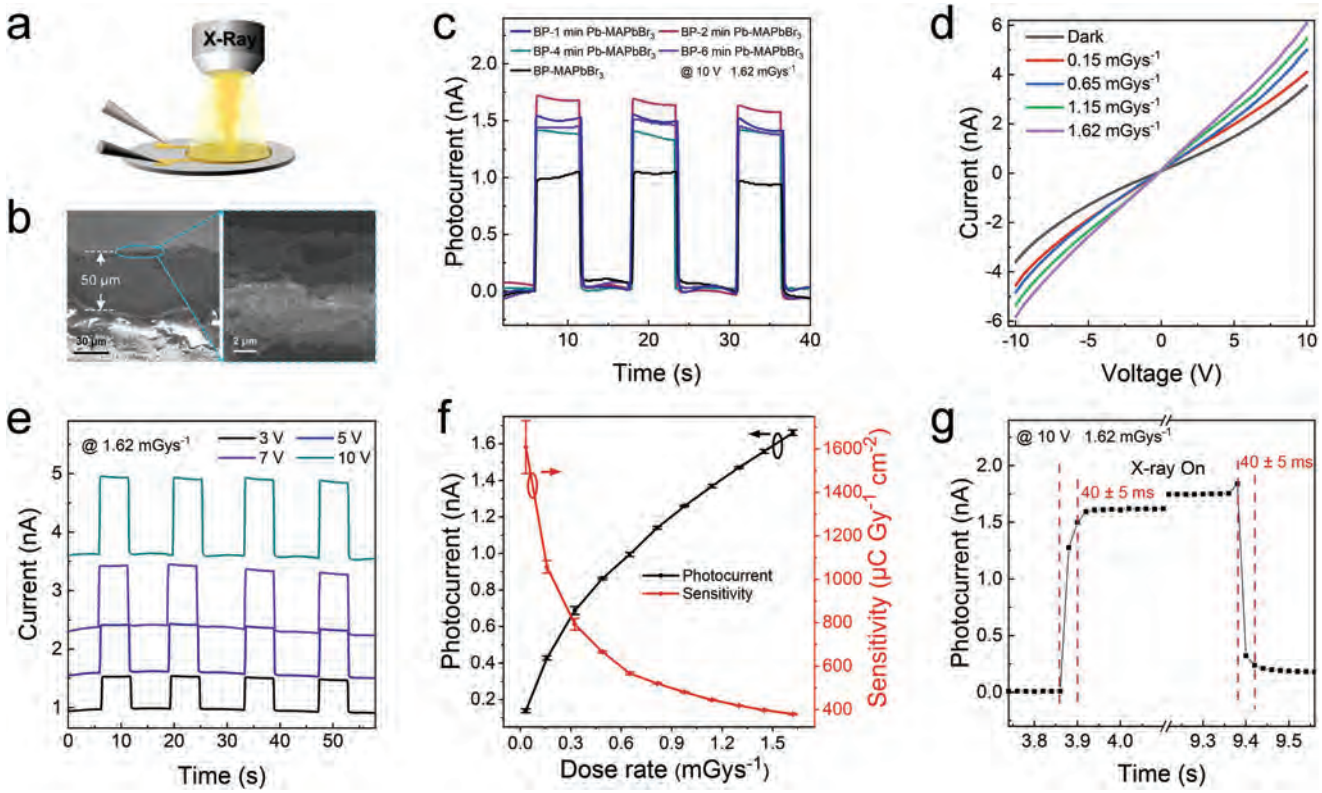

Figure 4. a) Schematic of the BP-Pb-MAPbBr$_3$-based X-ray detector prepared on the organic filter membrane and the X-ray beam was provided by a Rh-tube with 50 kV of accelerating voltage and current of 5–200 μA, b) cross-section of the film, c) photocurrents of the devices with the BP-MAPbBr$_3$ and BP-Pb-MAPbBr$_3$ heterostructures at 10 V bias voltage for a 1.62 mGys^{-1} dose rate, d) current-voltage curves of the device composed of the BP-2 min Pb-MAPbBr$_3$ heterostructure for different X-ray dose rates at voltages between −10 and 10 V, e) device response at different biases for a 1.62 mGys^{-1} dose rate, f) X-ray photocurrents and sensitivity at 10 V for different dose rates, and g) single X-ray response at 10 V for a 1.62 mGys^{-1} dose rate.

active phase in our heterostructure. The sensitivity increases with decreased dose rates and the highest sensitivity of 1609 ± 122 μC Gy−1cm−2 is achieved at 10 V by this X-ray detector for a 32 μGys^{-1} X-ray dose rate and photocurrent ≈0.14 nA. In fact, the sensitivity is more than 80 times higher than that of commercial amorphous Se (1-20 μC Gy^{-1} cm^{-2}).[32] A signal-to-noise ratio of 3 is crucial to X-ray detectors and the minimum detectable dose is expressed by the limit of detection (LoD). As shown in Figure S13 (Supporting Information), the LoD of the BP-2 min Pb-MAPbBr3 detector is calculated to be 3 μGys^{-1}, which is much smaller than dose rates required for most medical applications like skull, dental and chest radiology (about a fifteenth of the medical chest X-ray dose rate).[19,21,22,45,46] Relatively fast rise (reaching 90%) and fall (reaching 10%) times of both 40 ± 5 ms are also accomplished confirming the excellent detection properties. However, the sensitivity or LoD is smaller than those well designed flexible X-ray detectors,[47–49] which is most likely due to the charge transfer resistance between the restacked 2D heterostructures. Noteworthy, this work concerns the heterostructure design and fabrication strategy employed here, which allows to be extended to other types of heterostructures and have great potential in large-area, flexible, and sensitive X-ray detection applications.

To demonstrate the application potential, the flexibility and durability of the X-ray detector constructed with the BP-Pb-MAPbBr3 heterostructure are investigated. Compared to the flat form, the dark current decreases with bending radii (**Figure 5**a), and this phenomenon may be caused by stress or reduced incident ray reported previously.[19] Nonetheless, the photocurrents of the device decay only slightly with bending (Figure 5b). The mechanical flexibility of the detector is further verified by bending them multiple times with bending radius of 10 mm (strain of 0.75%). As shown in Figure 5c, the dark current decreases with increasing bending cycles possibly to impaction of residual stress. Nevertheless, it is noted that the photocurrents decay by only 10% after 200 bending cycles (Figure 5d). The film is examined by SEM and as shown in Figure S14a,b, (Supporting Information) a smooth uniform surface is observed before cycle and no change and cracks are observed after bending for 200 cycles, the close-up SEM image also shows the well bonded MAPbBr3 crystals on BP. While the pure MAPbBr3 film presents lots of cracks after only 5 bending cycles (Figure S14c,d, Supporting Information). These results indicate the good mechanical robustness of such BP-Pb-MAPbBr3 heterostructure based film. Besides, the stability of the BP-Pb-MAPbBr3 heterostructure under X-ray radiation is assessed. As shown in Figure S15a (Supporting Information), the XRD pattern of the BP-Pb-MAPbBr3 heterostructure has almost no change under continuous X-ray exposure indicating the excellent stability against X-ray radiation. As expected, the heterostructure based detector also exhibits good operation stability under a 1.62 mGys^{-1} dose rate for

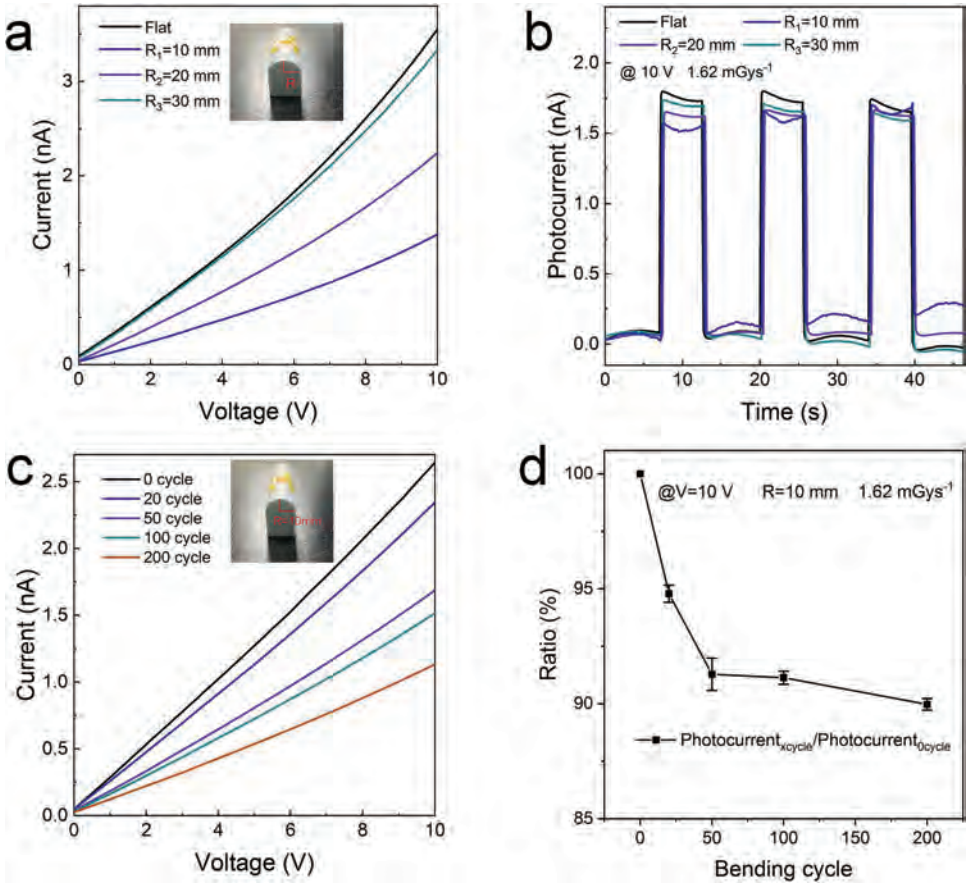

Figure 5. a) Current-voltage curves of the flexible device at bending radii of 10, 20, and 30 mm (strain of 0.25%, 0.38%, and 0.75%, respectively) with the inset showing the bending picture, b) photocurrents of the device at different bending radii and 10 V for a 1.62 $mGys^{-1}$ dose rate, c) current-voltage curves of the flexible device under flat condition after bending for 20, 50, 100, and 200 cycles with the inset showing the bending radius of 10 mm, and d) ratios of the photocurrents before and after bending.

3600 s (Figure S15b, Supporting Information). While such detector shows photocurrent degradation under storage at 25 °C with humidity of 60% – 70% (Figure S15c, Supporting Information), which is attributed to the weak water/oxygen-stability of BP and perovskite phase.

3. Conclusion

The BP-Pb-$MAPbBr_3$ heterostructure is synthesized based on an interfacial engineering strategy and can serve as active material via a simple vacuum filtration technique for direct, flexible, and high-sensitivity X-ray detectors. A Pb transition layer with a typical thickness of 0.6 nm is prepared on BP to enable epitaxial growth of high-quality pyramidal $MAPbBr_3$ nanocrystals by taking advantage of the high lattice matching. Owing to the strong bridging and anchoring ability of the Pb transition layer, the heterostructure is very strong mechanically. The X-ray detector fabricated with the BP-2 min Pb-$MAPbBr_3$ heterostructure and organic filter membrane shows excellent X-ray response and flexibility such as a high X-ray sensitivity of 1609 ± 122 μC Gy^{-1} cm^{-2}, fast response time of 40 ± 5 ms, as well as significant LoD down to 3 μGys^{-1}. This simple and planar device is bendable and durable, showing photocurrent degradation of only 10% after 200 bending cycles and good operation stability under X-ray radiation. The novel concept of fabricating a Pb transition layer for two-way bridging of BP and $MAPbBr_3$ can be extended to other types of heterostructures and the flexible X-ray detector consisting of BP-Pb-$MAPbBr_3$ has large potential in X-ray detection applications.

4. Experimental Section

Materials: The bulk BP crystals were purchased from MoPhos Technology Co. Ltd. (China) and tetrabutylammonium bromide (TBAB, 99%) and lead bromide ($PbBr_2$, 99%) were bought from Shanghai Macklin Biochemical Technology Co., Ltd. (China). Methylammonium bromide (MABr, 99.99%) was obtained from GreatCell Solar Ltd and toluene (99%), isopropanol (IPA, 99%), and *N,N*-dimethylformamide (DMF, AR, 99%) were purchased from Shanghai Lingfeng Chemical Reagent Co. Ltd. (China). The organic filter membrane (0.2 μm) was acquired from Tianjin Jinteng Experimental Equipment Co., Ltd. (China). The gold particles (product No. Au11474 3*3 mm) used to prepare the gold electrodes were purchased from Zhong Nuo New Materials Co., Ltd. (Beijing, China).

Synthesis of BP-Pb-MAPbBr3 heterostructures: The BP-Pb-MAPbBr3 heterostructures were synthesized in four stages including electrochemical intercalation, activation, deposition, and epitaxial growth.

Stage 1: The electrolyte solution was prepared by dissolving 5 mmol TBAB in 25 mL DMF. 1.3 mg of the bulk BP crystal immersed in the solution served as the cathode and a Pt plate was the anode. The first electrochemical intercalation step proceeded under a voltage of 4 V for 1 min.

Stage 2: Diluted HNO3 (1:4, 500 µL) was added to the electrolyte solution and activation proceeded at an applied voltage to −5 V for 1 min.

Stage 3: The DMF solution containing 1 mmol $PbBr_2$ (25 mL) was added to the electrolyte solution. Deposition was carried out at a voltage of 12 V for 1, 2, 4, and 6 min, respectively. The samples were collected, dispersed in 5 mL of the DMF solution, and sonicated for 10 min. The samples were centrifuged and washed with DMF three times. Afterward, the samples were redispersed in 3.5 mL of the DMF solution for further use. The BP-Pb composites were denoted as BP-1 min Pb, BP-2 min Pb, BP-4 min Pb and BP-6 min Pb sheets, respectively.

Stage 4: BP-Pb-$MAPbBr_3$: 0.5 mmol MABr and 0.5 mmol $PbBr_2$ were dissolved in 0.5 mL DMF solution to prepare the perovskite precursor. It was mixed with 1 mL of the BP-Pb solution in a 10 mL glass bottle and heated to 80 °C for 15 min. The mixture was centrifuged at 4 800 rpm for 2 min and the precipitate was collected, washed with toluene and IPA three times, and redispersed in IPA for further use. The samples prepared with BP-1 min Pb, BP-2 min Pb, BP-4 min Pb, and BP-6 min Pb were designated as BP-1 min Pb-$MAPbBr_3$, BP-2 min Pb-$MAPbBr_3$, BP-4 min Pb-$MAPbBr_3$, and BP-6 min Pb-$MAPbBr_3$, respectively.

BP-MAPbBr3: The perovskite growth process was the same as that of BP-Pb-MAPbBr3 except that the BP sheets were electrochemically exfoliated without Pb deposition.

Device Fabrication: An 80 nm thick Au interdigital electrode was prepared on an organic membrane by heat evaporation plating in a vacuum. The devices were prepared by vacuum filtration. Before filtration, the BP-Pb-$MAPbBr_3$ IPA dispersion was sonicated for 5 min.

Characterization: The scanning electron microscopy (SEM) images were obtained on the ZEISS SUPRA 55 (Carl Zeiss, Germany) field-emission scanning electron microscope, and transmission electron microscopy (TEM) and high-resolution TEM (HR-TEM) were performed on the Talos F200X transmission electron microscope (FEI, USA) at an acceleration voltage of 200 kV. The surface morphology was examined on the Cypher S AFM (Asylum Research, USA) and XRD was carried out the Rigaku Smartlab 3 kW X-ray diffractometer with Cu K_α radiation ($\lambda = 1.54056$ Å, 40 kV, 30 mA, 5° min^{-1}). The XPS spectra were obtained on an ESCALAB 250Xi electron spectrometer (Thermo Fisher Scientific) and the UV–vis absorption spectra were acquired on a UV–vis spectrophotometer (UV-1800, Shimadzu). Raman scattering was carried out on the high-resolution confocal Raman microscope equipped with a 633 nm laser (Horiba Jobin Yvon LabRam HR-VIS). An Amptek miniature X-ray tube system, Mini-X2-Rh, was used as the X-ray source and the accelerating voltage was 50 kV. Different doses were obtained by changing the currents and calibrating was conducted with a commercial dose meter (X2 CT Sensor, Unfors RaySafe). The measurement was performed in the air and in darkness. The PDA FS380 semiconductor analyzer was employed in the current/voltage measurement.

Supporting Information

Supporting Information is available from the Wiley Online Library or from the author.

Acknowledgements

H.H., Y.Z., and C.L. contributed equally to this work. This work was supported by the National Natural Science Foundation of China (12235006, 21975280), Shenzhen Science and Technology Program Grant (RCJC20200714114435061, ZDSYS20220527171406014), General Program of Natural Science Foundation of Guangdong Province (2022A1515011959), Young Elite Scientist Sponsorship Program by CAST (No. YESS20210226), Youth Innovation Promotion Association Chinese Academy of Sciences (2020354), City University of Hong Kong Donation Research Grant (DON-RMG No. 9229021), City University of Hong Kong Strategic Research Grant (SRG No. 7005505), as well as City University of Hong Kong Donation Grant (No. 9220061).

Conflict of Interest

The authors declare no conflict of interest.

Data Availability Statement

The data that support the findings of this study are available from the corresponding author upon reasonable request.

Keywords

black phosphorus, epitaxial growth, flexible X-ray detectors, interfacial engineering, perovskite

Received: April 17, 2023
Revised: June 12, 2023
Published online: July 20, 2023

[1] B. Guo, Q.-l. Xiao, S.-h. Wang, H. Zhang, *Laser Photonics Rev.* **2019**, *13*, 1800327.
[2] F. Yi, H. Ren, J. Shan, X. Sun, D. Wei, Z. Liu, *Chem. Soc. Rev.* **2018**, *47*, 3152.
[3] K. S. Novoselov, A. Mishchenko, A. Carvalho, A. H. Castro Neto, *Science* **2016**, *353*, aac9439.
[4] S. Haastrup, M. Strange, M. Pandey, T. Deilmann, P. S. Schmidt, N. F. Hinsche, M. N. Gjerding, D. Torelli, P. M. Larsen, A. C. Riis-Jensen, J. Gath, K. W. Jacobsen, J. Jørgen Mortensen, T. Olsen, K. S. Thygesen, *2D Mater.* **2018**, *5*, 042002.
[5] E. S. Penev, N. Marzari, B. I. Yakobson, *ACS Nano* **2021**, *15*, 5959.
[6] G. R. Bhimanapati, Z. Lin, V. Meunier, Y. Jung, J. Cha, S. Das, D. Xiao, Y. Son, M. S. Strano, V. R. Cooper, L. Liang, S. G. Louie, E. Ringe, W. Zhou, S. S. Kim, R. R. Naik, B. G. Sumpter, H. Terrones, F. Xia, Y. Wang, J. Zhu, D. Akinwande, N. Alem, J. A. Schuller, R. E. Schaak, M. Terrones, J. A. Robinson, *ACS Nano* **2015**, *9*, 11509.
[7] X. Feng, A. D. Schlüter, *Angew. Chem., Int. Ed.* **2018**, *57*, 13748.
[8] H. Xu, H. Shang, C. Wang, Y. Du, *Small* **2021**, *17*, 2005092.
[9] Y. Gogotsi, B. Anasori, *ACS Nano* **2019**, *13*, 8491.
[10] S. Manzeli, D. Ovchinnikov, D. Pasquier, O. V. Yazyev, A. Kis, *Nat. Rev. Mater.* **2017**, *2*, 17033.
[11] H. Liu, Y. Du, Y. Deng, P. D. Ye, *Chem. Soc. Rev.* **2015**, *44*, 2732.
[12] X. Cai, Y. Luo, B. Liu, H.-M. Cheng, *Chem. Soc. Rev.* **2018**, *47*, 6224.
[13] B. Pradhan, S. Das, J. Li, F. Chowdhury, J. Cherusseri, D. Pandey, D. Dev, A. Krishnaprasad, E. Barrios, A. Towers, A. Gesquiere, L. Tetard, T. Roy, J. Thomas, *Sci. Adv.* **2020**, *6*, eaay5225.
[14] J. Zhang, Y. Huang, Z. Tan, T. Li, Y. Zhang, K. Jia, L. Lin, L. Sun, X. Chen, Z. Li, C. Tan, J. Zhang, L. Zheng, Y. Wu, B. Deng, Z. Chen, Z. Liu, H. Peng, *Adv. Mater.* **2018**, *30*, 1803194.
[15] J. Wang, J. Han, X. Chen, X. Wang, *Info. Mat* **2019**, *1*, 33.
[16] W. Yu, K. Gong, Y. Li, B. Ding, L. Li, Y. Xu, R. Wang, L. Li, G. Zhang, S. Lin, *Small* **2022**, *18*, 2105383.
[17] W. Pan, H. Wu, J. Luo, Z. Deng, C. Ge, C. Chen, X. Jiang, W.-J. Yin, G. Niu, L. Zhu, L. Yin, Y. Zhou, Q. Xie, X. Ke, M. Sui, J. Tang, *Nat. Photonics* **2017**, *11*, 726.
[18] J. Zhao, L. Zhao, Y. Deng, X. Xiao, Z. Ni, S. Xu, J. Huang, *Nat. Photonics* **2020**, *14*, 612.

[19] J. Liu, B. Shabbir, C. Wang, T. Wan, Q. Ou, P. Yu, A. Tadich, X. Jiao, D. Chu, D. Qi, D. Li, R. Kan, Y. Huang, Y. Dong, J. Jasieniak, Y. Zhang, Q. Bao, *Adv. Mater.* **2019**, *31*, 1901644.
[20] H. M. Thirimanne, K. D. G. I. Jayawardena, A. J. Parnell, R. M. I. Bandara, A. Karalasingam, S. Pani, J. E. Huerdler, D. G. Lidzey, S. F. Tedde, A. Nisbet, C. A. Mills, S. R. P. Silva, *Nat. Commun.* **2018**, *9*, 2926.
[21] A. Ciavatti, R. Sorrentino, L. Basiricò, B. Passarella, M. Caironi, A. Petrozza, B. Fraboni, *Adv. Funct. Mater.* **2021**, *31*, 2009072.
[22] C. Liang, S. Zhang, L. Cheng, J. Xie, F. Zhai, Y. He, Y. Wang, Z. Chai, S. Wang, *Angew. Chem., Int. Ed.* **2020**, *59*, 11856.
[23] Z. Li, S. Chang, H. Zhang, Y. Hu, Y. Huang, L. Au, S. Ren, *Nano Lett.* **2021**, *21*, 6983.
[24] Y.-H. Lin, N. Sakai, P. Da, J. Wu, H. C. Sansom, A. J. Ramadan, S. Mahesh, J. Liu, R. D. J. Oliver, J. Lim, L. Aspitarte, K. Sharma, P. K. Madhu, A. B. Morales-Vilches, P. K. Nayak, S. Bai, F. Gao, C. R. M. Grovenor, M. B. Johnston, J. G. Labram, J. R. Durrant, J. M. Ball, B. Wenger, B. Stannowski, H. J. Snaith, *Science* **2020**, *369*, 96.
[25] K. Lin, J. Xing, L. N. Quan, F. P. G. de Arquer, X. Gong, J. Lu, L. Xie, W. Zhao, D. Zhang, C. Yan, W. Li, X. Liu, Y. Lu, J. Kirman, E. H. Sargent, Q. Xiong, Z. Wei, *Nature* **2018**, *562*, 245.
[26] B. R. Sutherland, E. H. Sargent, *Nat. Photonics* **2016**, *10*, 295.
[27] X. He, Y. Deng, D. Ouyang, N. Zhang, J. Wang, A. A. Murthy, I. Spanopoulos, S. M. Islam, Q. Tu, G. Xing, Y. Li, V. P. Dravid, T. Zhai, *Chem. Rev.* **2023**, *123*, 1207.
[28] L. Wang, X. Zou, J. Lin, J. Jiang, Y. Liu, X. Liu, X. Zhao, Y. F. Liu, J. C. Ho, L. Liao, *ACS Nano* **2019**, *13*, 4804.
[29] Q. Zhou, J. Duan, X. Yang, Y. Duan, Q. Tang, *Angew. Chem., Int. Ed.* **2020**, *59*, 21997.
[30] W. Wei, Y. Zhang, Q. Xu, H. Wei, Y. Fang, Q. Wang, Y. Deng, T. Li, A. Gruverman, L. Cao, J. Huang, *Nat. Photonics* **2017**, *11*, 315.
[31] A. Glushkova, P. Andričević, R. Smajda, B. Náfrádi, M. Kollár, V. Djokić, A. Arakcheeva, L. Forró, R. Pugin, E. Horváth, *ACS Nano* **2021**, *15*, 4077.
[32] P. Zhang, Y. Hua, Y. Xu, Q. Sun, X. Li, F. Cui, L. Liu, Y. Bi, G. Zhang, X. Tao, *Adv. Mater.* **2022**, *34*, 2106562.
[33] J. Yu, M. Wang, S. Lin, *ACS Nano* **2016**, *10*, 11044.
[34] W. Pan, B. Yang, G. Niu, K.-H. Xue, X. Du, L. Yin, M. Zhang, H. Wu, X.-S. Miao, J. Tang, *Adv. Mater.* **2019**, *31*, 1904405.
[35] S. Zhou, C. Bao, B. Fan, H. Zhou, Q. Gao, H. Zhong, T. Lin, H. Liu, P. Yu, P. Tang, S. Meng, W. Duan, S. Zhou, *Nature* **2023**, *614*, 75.
[36] F. Xia, H. Wang, J. C. M. Hwang, A. H. C. Neto, L. Yang, *Nat Rev Phys* **2019**, *1*, 306.
[37] S. Yuan, D. Naveh, K. Watanabe, T. Taniguchi, F. Xia, *Nat. Photonics* **2021**, *15*, 601.
[38] J.-Y. Wang, Y. Li, Z.-Y. Zhan, T. Li, L. Zhen, C.-Y. Xu, *Appl. Phys. Lett.* **2016**, *108*, 013104.
[39] H. Huang, L. He, W. Zhou, G. Qu, J. Wang, N. Yang, J. Gao, T. Chen, P. K. Chu, X.-F. Yu, *Biomaterials* **2018**, *171*, 12.
[40] T. Wu, Z. Ma, Y. He, X. Wu, B. Tang, Z. Yu, G. Wu, S. Chen, N. Bao, *Angew. Chem., Int. Ed.* **2021**, *60*, 10366.
[41] Q. Zhang, Y.-H. Song, J.-M. Hao, Y.-F. Lan, L.-Z. Feng, X.-C. Ru, J.-J. Wang, K.-H. Song, J.-N. Yang, T. Chen, H.-B. Yao, *J. Am. Chem. Soc.* **2022**, *144*, 8162.
[42] X. Geng, P. Zhang, J. Ren, G.-H. Dun, Y. Li, J. Jin, C. Wang, X. Wu, D. Xie, H. Tian, Y. Yang, T.-L. Ren, *InfoMat* **2022**, *4*, e12347.
[43] J. Xing, X. Zheng, Z. Yu, Y. Lei, L. Hou, Y. Zou, C. Zhao, B. Wang, H. Yu, D. Pan, Y. Zhai, J. Cheng, D. Zhou, S. Qu, J. Yang, R. A. Ganeev, W. Yu, C. Guo, *Adv. Opt. Mater.* **2018**, *6*, 1800411.
[44] Y. Wang, F. Yang, X. Li, F. Ru, P. Liu, L. Wang, W. Ji, J. Xia, X. Meng, *Adv. Funct. Mater.* **2019**, *29*, 1904913.
[45] K. Liu, Y. Bian, J. Kuang, X. Huang, Y. Li, W. Shi, Z. Zhu, G. Liu, M. Qin, Z. Zhao, X. Li, Y. Guo, Y. Liu, *Adv. Mater.* **2022**, *34*, 2107304.
[46] J. Billinger, R. Nowotny, P. Homolka, *Eur Radiol* **2010**, *20*, 1572.
[47] X. Liu, H. Li, Q. Cui, S. Wang, C. Ma, N. Li, N. Bu, T. Yang, X. Song, Y. Liu, Z. Yang, K. Zhao, S. Liu, *Angew. Chem., Int. Ed.* **2022**, *61*, e202209320.
[48] J. Zhao, X. Wang, Y. Ding, Z. Wei, Y. Xu, Y. Pan, Y. Li, B. S. Bae, M. Furuta, Z. Zhu, Q. Li, J. Zhou, X. Zhang, W. Lei, *J. Mater. Chem. A* **2023**, *11*, 9049.
[49] Z. Li, G. Peng, H. Chen, C. Shi, Z. Li, Z. Jin, *Angew. Chem., Int. Ed.* **2022**, *61*, e202207198.

NANO · MICRO small

Supporting Information

for *Small*, DOI 10.1002/smll.202303229

Interfacial Engineering Enables Perovskite Heteroepitaxial Growth on Black Phosphorus for Flexible X-ray Detectors

Hao Huang, Ying Zheng, Chang Liu, Zhenyu Zhang, Ming Gao, Jiahong Wang, Yanliang Liu, Paul K. Chu and Xue-Feng Yu**

WILEY-VCH

Supporting Information

Interfacial Engineering Enables Perovskite Heteroepitaxial Growth on Black Phosphorus for Flexible X-ray Detectors

Hao Huang, Ying Zheng, Chang Liu, Zhenyu Zhang, Ming Gao, Jiahong Wang, Yanliang Liu, Paul K. Chu and Xue-Feng Yu**

H. Huang, Y. Zheng, Z. Zhang, M. Gao, J. Wang, Y. Liu, X.-F. Yu

Shenzhen Key Laboratory of Micro/Nano Biosensing, Shenzhen Institute of Advanced Technology, Chinese Academy of Sciences, Shenzhen, 518055, P. R. China

E-mail: hao.huang@siat.ac.cn (H. Huang); xf.yu@siat.ac.cn (X.-F. Yu)

H. Huang, C. Liu, J. Wang, X.-F. Yu

Hubei Three Gorges Laboratory, Yichang, Hubei, 443007, P. R. China

Y. Zheng

Nano Science and Technology Institute, University of Science and Technology of China, Suzhou, 215123, P. R. China

P. K. Chu

Department of Physics, Department of Materials Science and Engineering, and Department of Biomedical Engineering, City University of Hong Kong, Tat Chee Avenue, Kowloon, Hong Kong, China

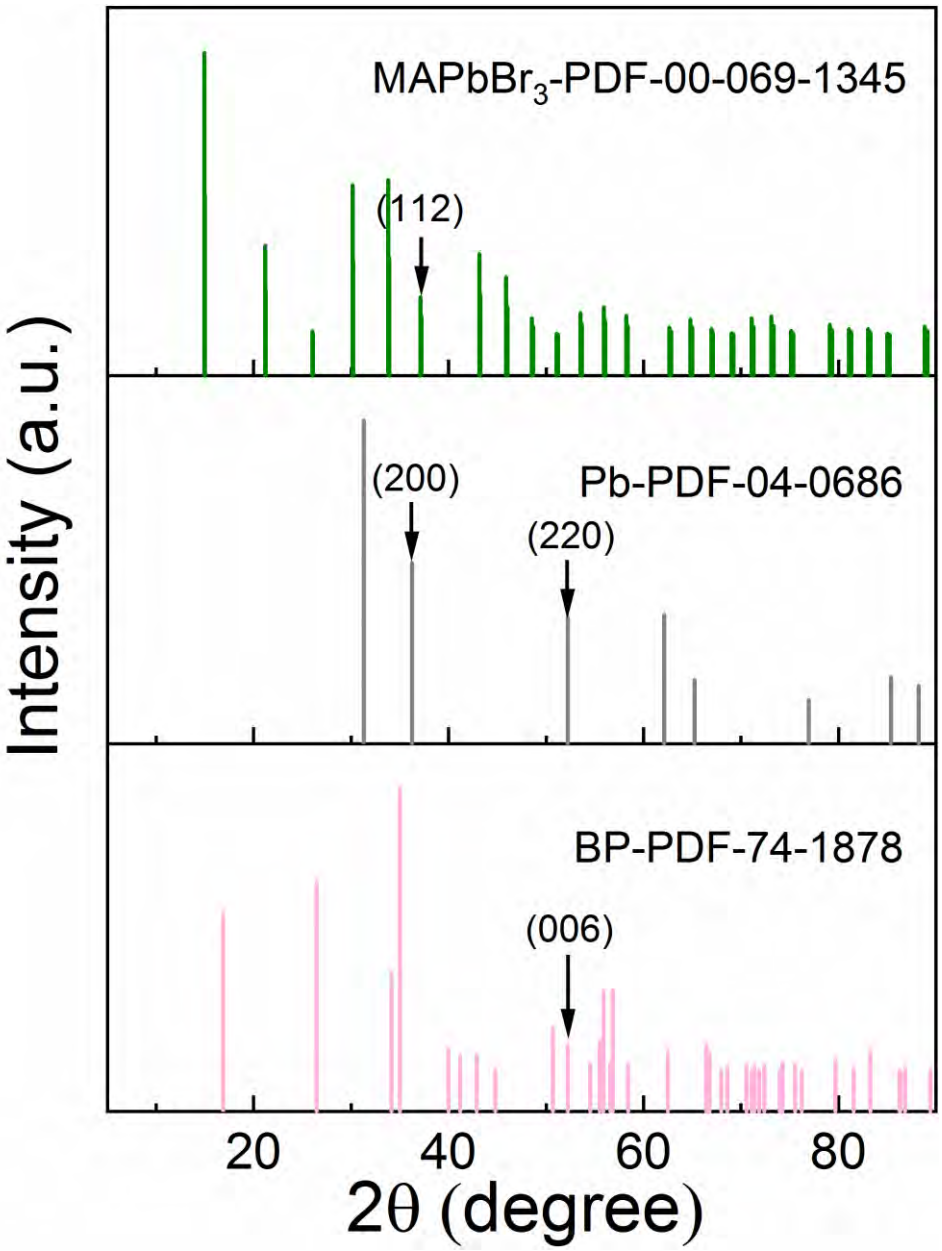

Figure S1. XRD patterns of BP, Pb, and $MAPbBr_3$.

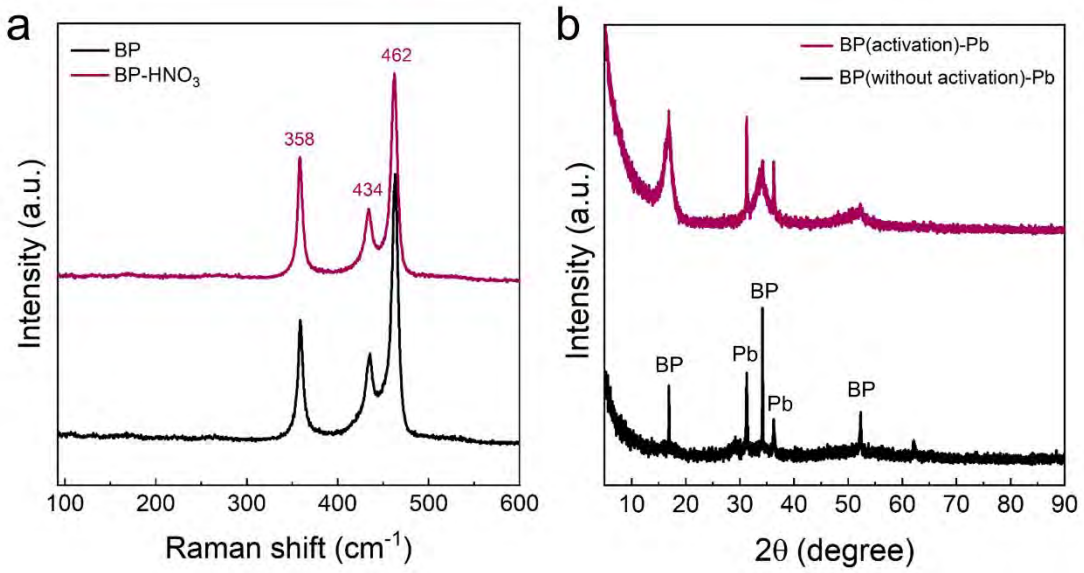

Figure S2. (a) Raman scattering spectra of electrochemical exfoliated BP with/without HNO_3 and (b) XRD patterns of BP-Pb with/without HNO_3 activation.

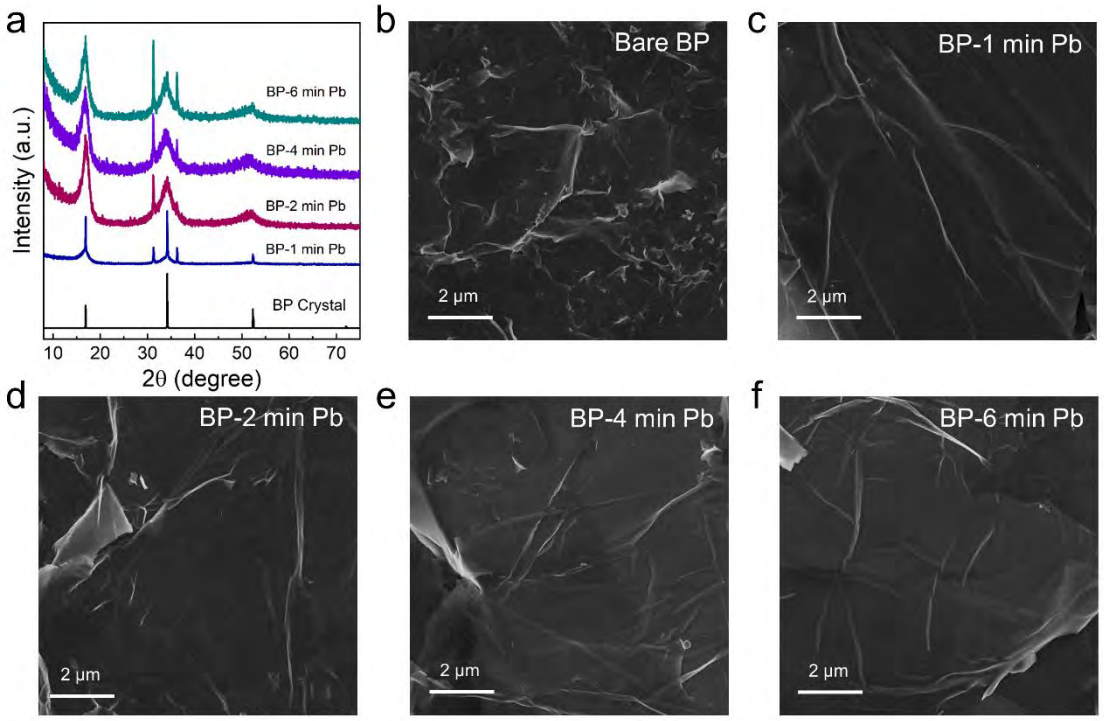

Figure S3. (a) XRD patterns of the BP crystal and samples with Pb deposited together with electrochemical exfoliation for 1, 2, 4, and 6 min designated as BP-1 min Pb, BP-2 min Pb, BP-4 min Pb, and BP-6 min Pb; (b) SEM image of the exfoliated BP without deposition of Pb; (c-f) SEM images of BP-1 min Pb, BP-2 min Pb, BP-4 min Pb, and BP-6 min Pb sheets, respectively.

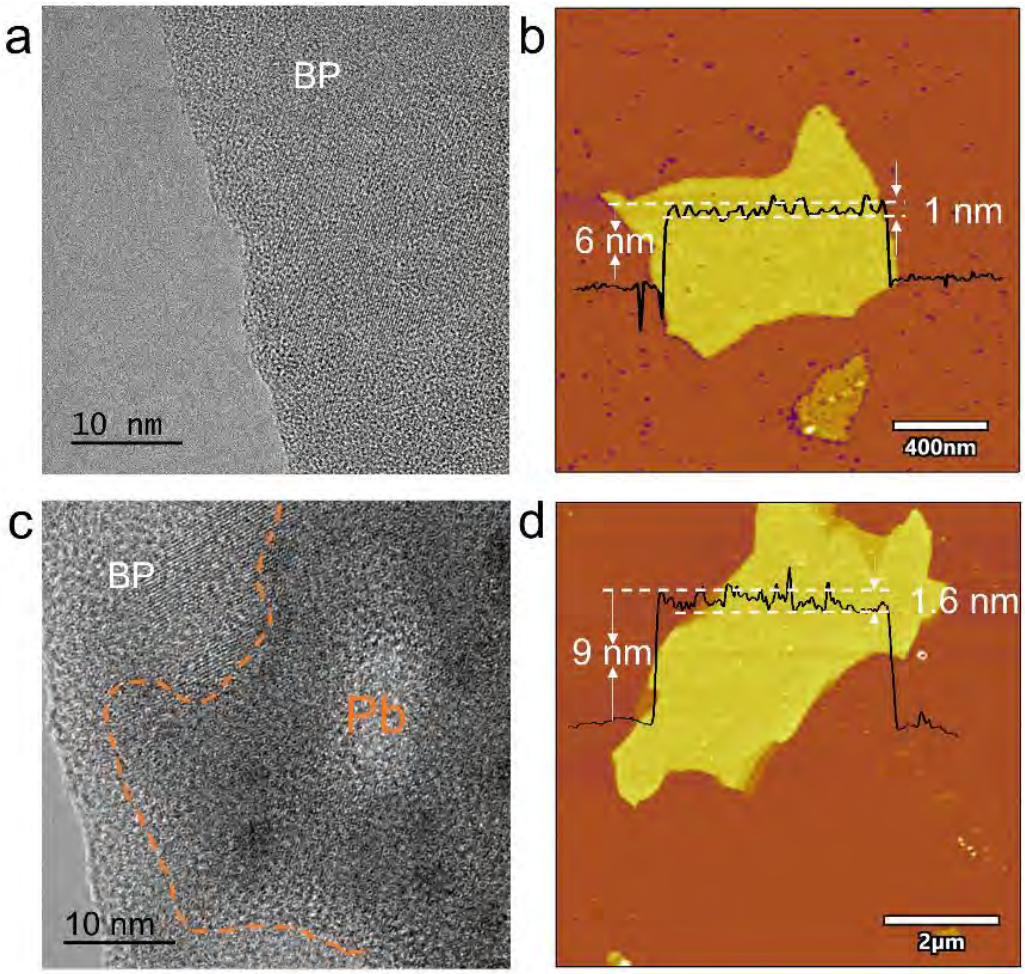

Figure S4. (a, b) TEM image and AFM image of one bare BP sheet and (c, d) TEM image and AFM image of one BP-2 min Pb.

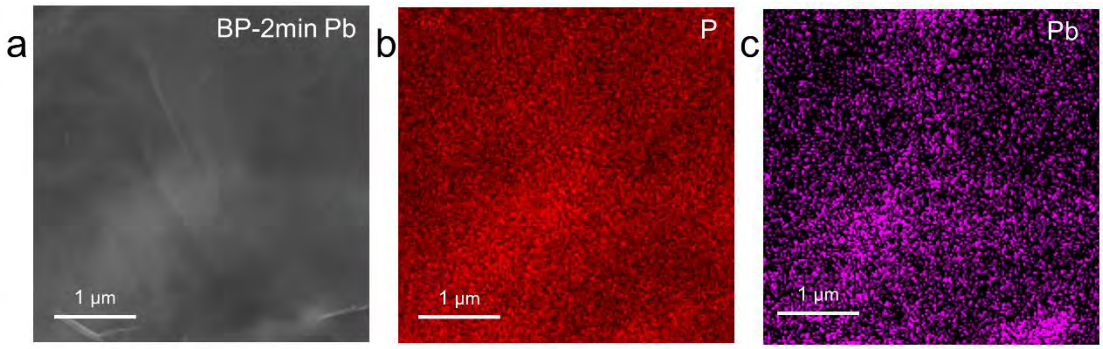

Figure S5. (a) SEM image of BP-2 min Pb and (b, c) EDS element maps of P and Pb.

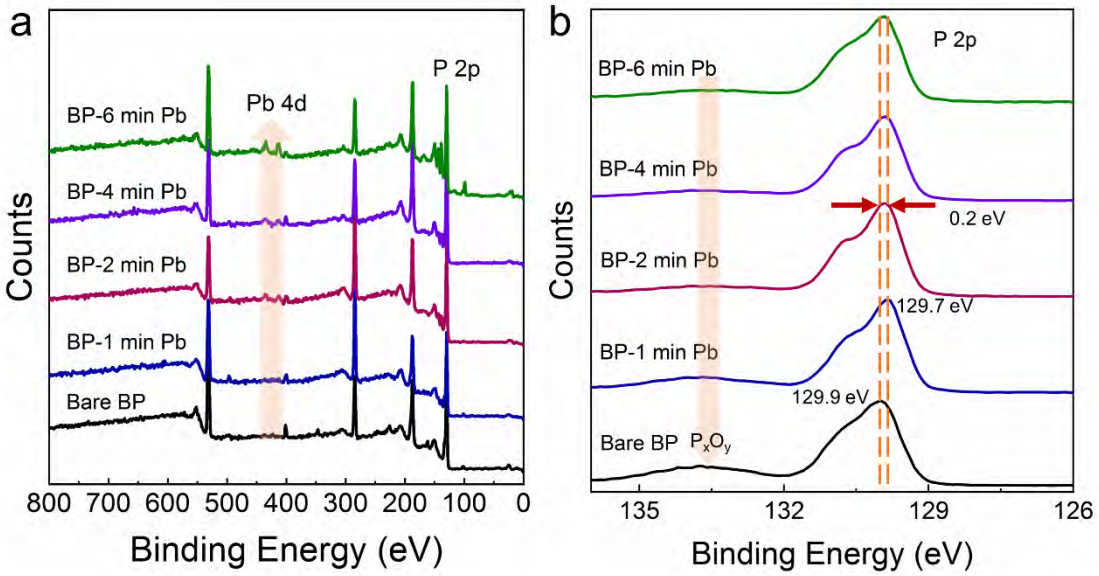

Figure S6. (a) XPS surveys of the bare BP, BP-1 min Pb, BP-2 min Pb, BP-4 min Pb, and BP-6 min Pb and (b) Corresponding high-resolution P 2*p* spectra.

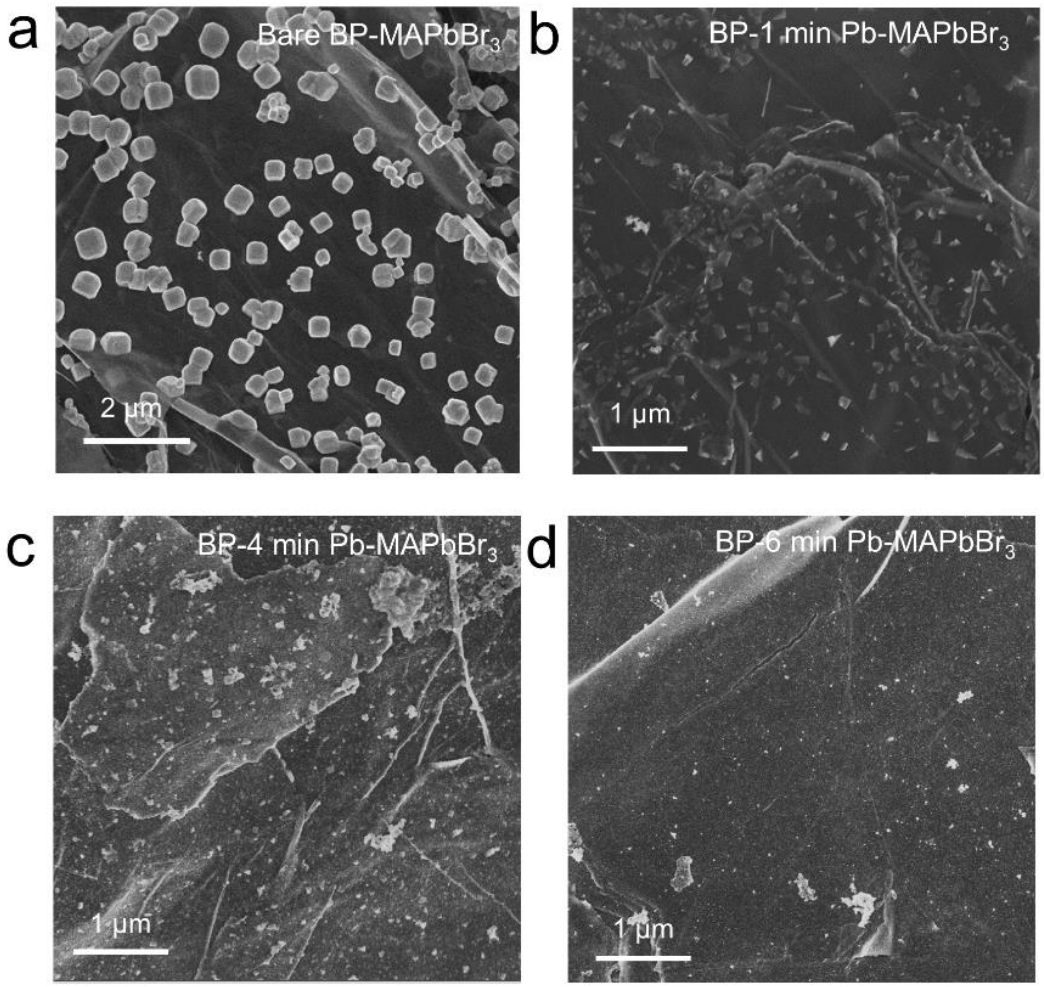

Figure S7. SEM images of the heterostructures of bare BP, BP-1 min Pb-$MAPbBr_3$, BP-4 min Pb-$MAPbBr_3$, and BP-6 min Pb-$MAPbBr_3$ sheets.

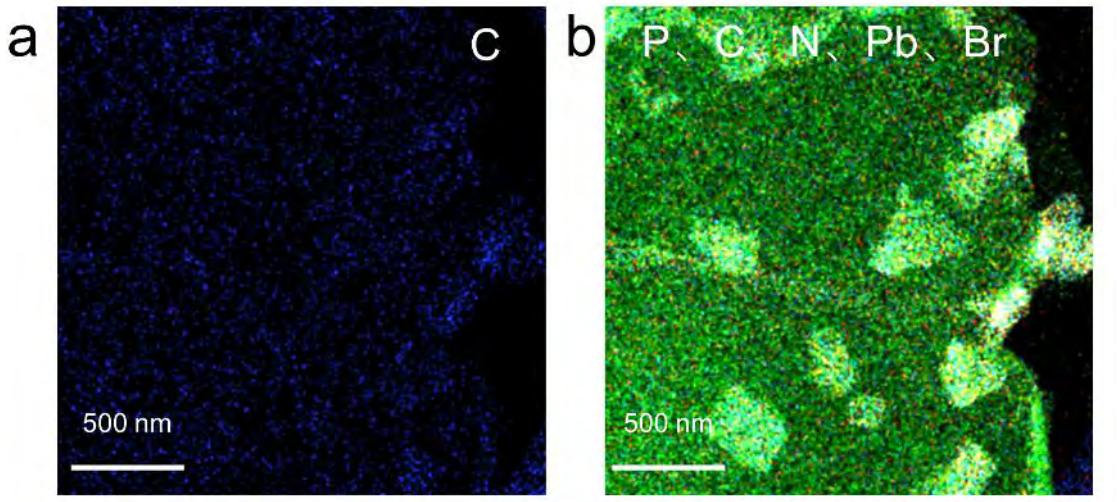

Figure S8. EDS maps.

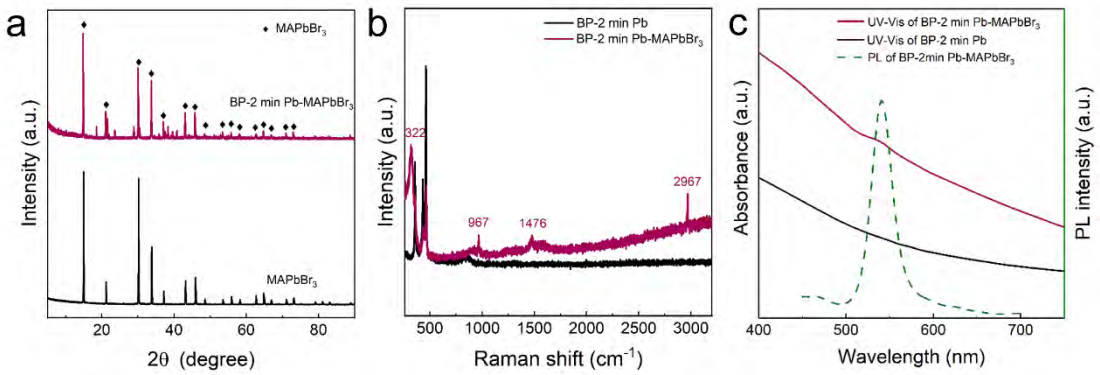

Figure S9. (a) XRD spectra of the BP-2 min Pb-$MAPbBr_3$ heterostructure and $MAPbBr_3$ powder, (b) Raman scattering spectra of the BP-2 min Pb sheet and BP-2 min Pb-$MAPbBr_3$ heterostructure, and (c) Absorption spectra of the BP-2 min Pb sheet and BP-2 min Pb-$MAPbBr_3$ heterostructure together with the PL spectrum of BP-2 min Pb-$MAPbBr_3$.

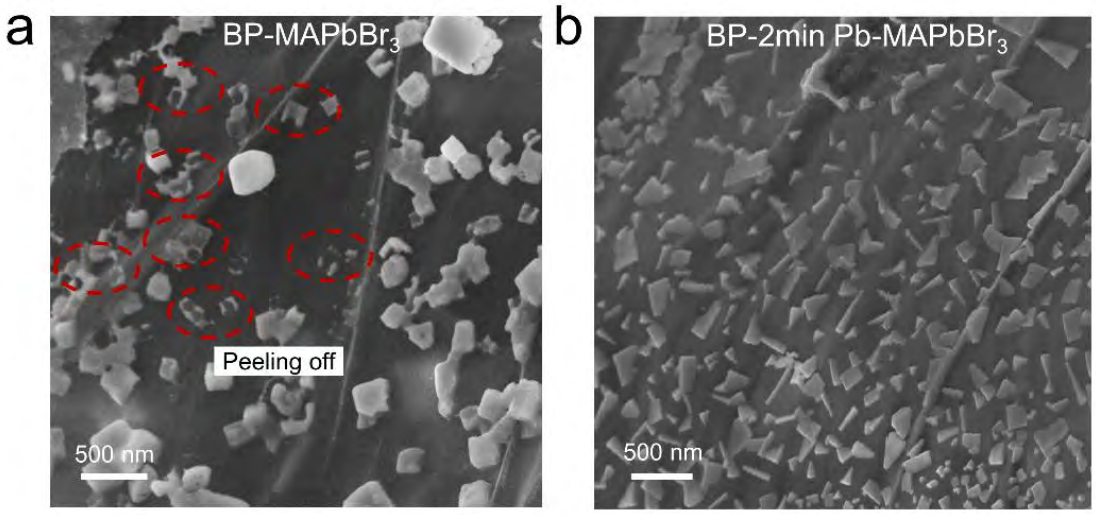

Figure S10. (a, b) SEM images of the BP-$MAPbBr_3$ and BP-2 min Pb-$MAPbBr_3$ heterostructures after washing with IPA three times.

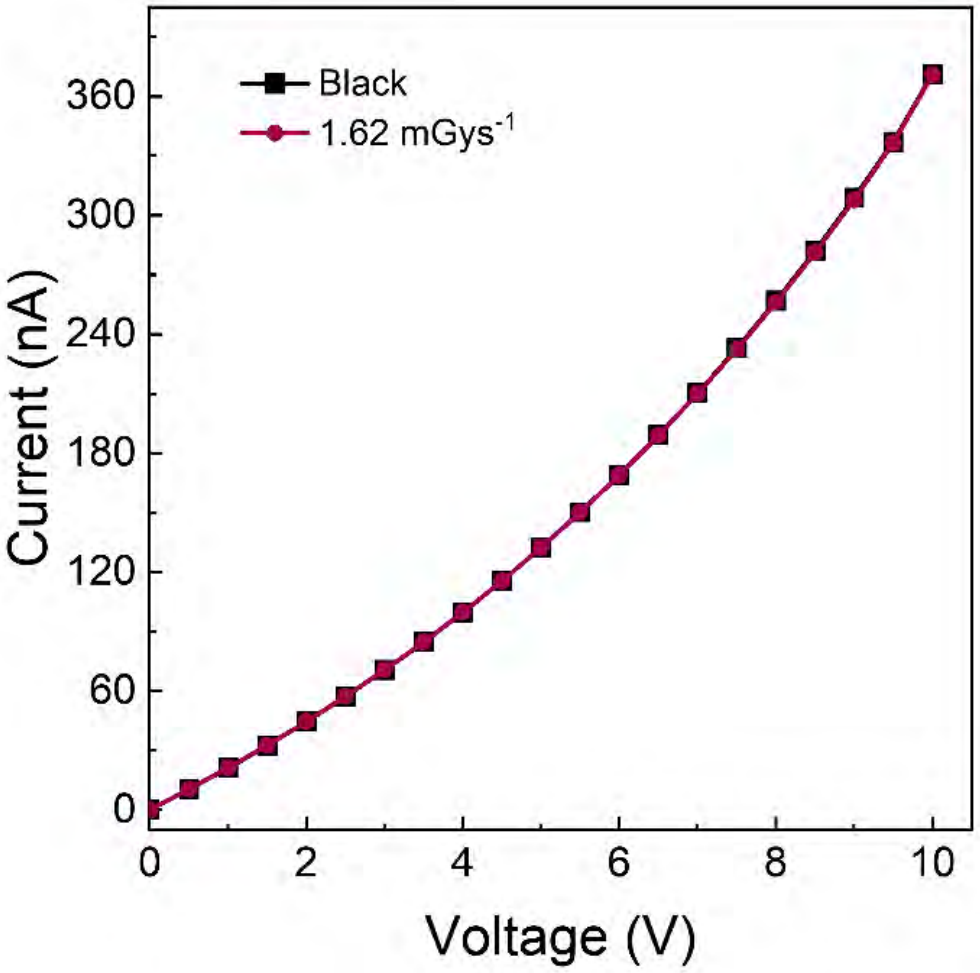

Figure S11. Current-voltage curve of the device fabricated with bare BP at bias voltages between 0 and 10 V (black: without X-ray and red: 1.62 $mGys^{-1}$ dose rate).

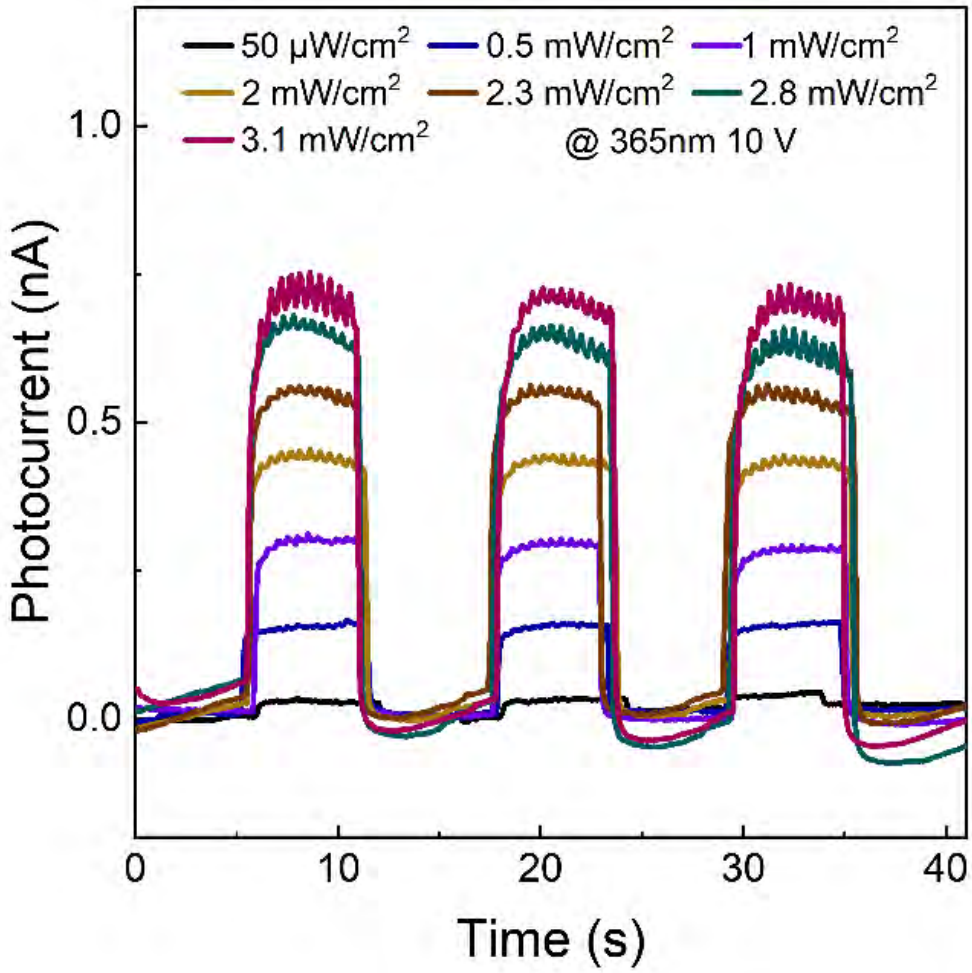

Figure S12. Photocurrents versus power density under 365 nm UV at 10 V.

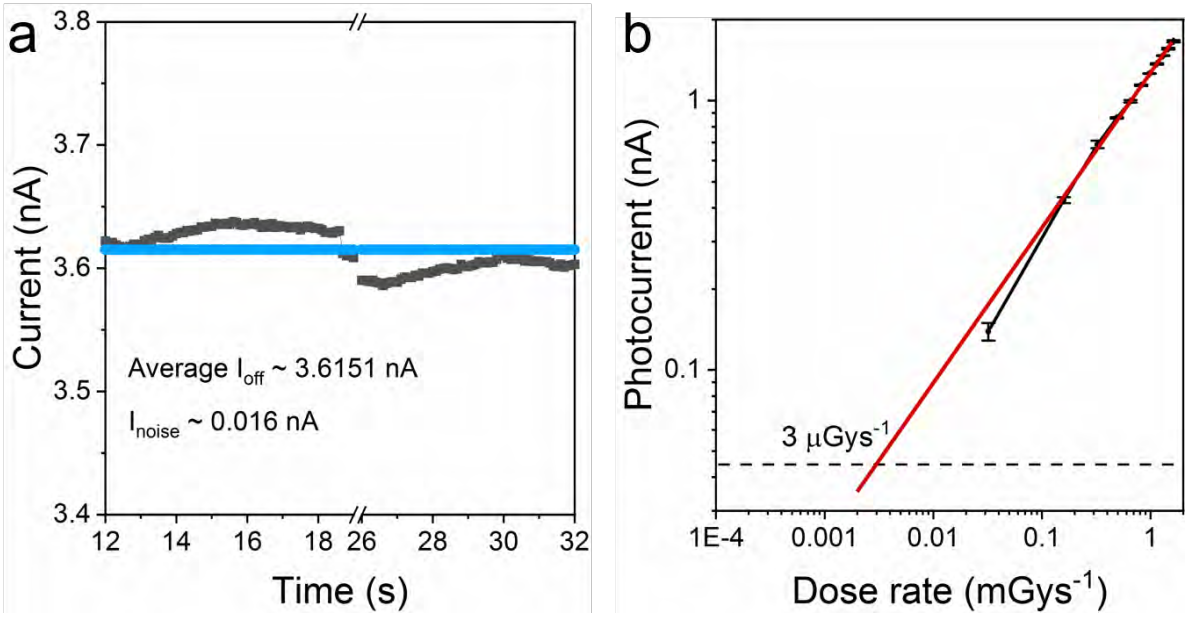

Figure S13. (a) Dark current in Fig. 4e (10 V, 12-19 s and 26-32 s). (b) Photocurrents versus dose rates for the experimental data (dark dots), linear fit (red line), and signal-to-noise limit of 3 (black dashed line). The log-log scale reveals that LoD is equal to 3 μGys^{-1}.

The dark current in Fig. 4e (10 V, 12-19 s and 26-32 s) was used to calculate the standard deviation, which served as the noise current (I_{noise}).[Nature Communications (2023) 14:626]

$$I_{noise} = \sqrt{\frac{1}{N}\sum_{i}^{N}(I_i - average\ I_{off})^2}$$

Thus, the I_{noise} was determined to be ~0.016 nA. 3 × SNR=3 × I_{noise} ~0.05 nA.

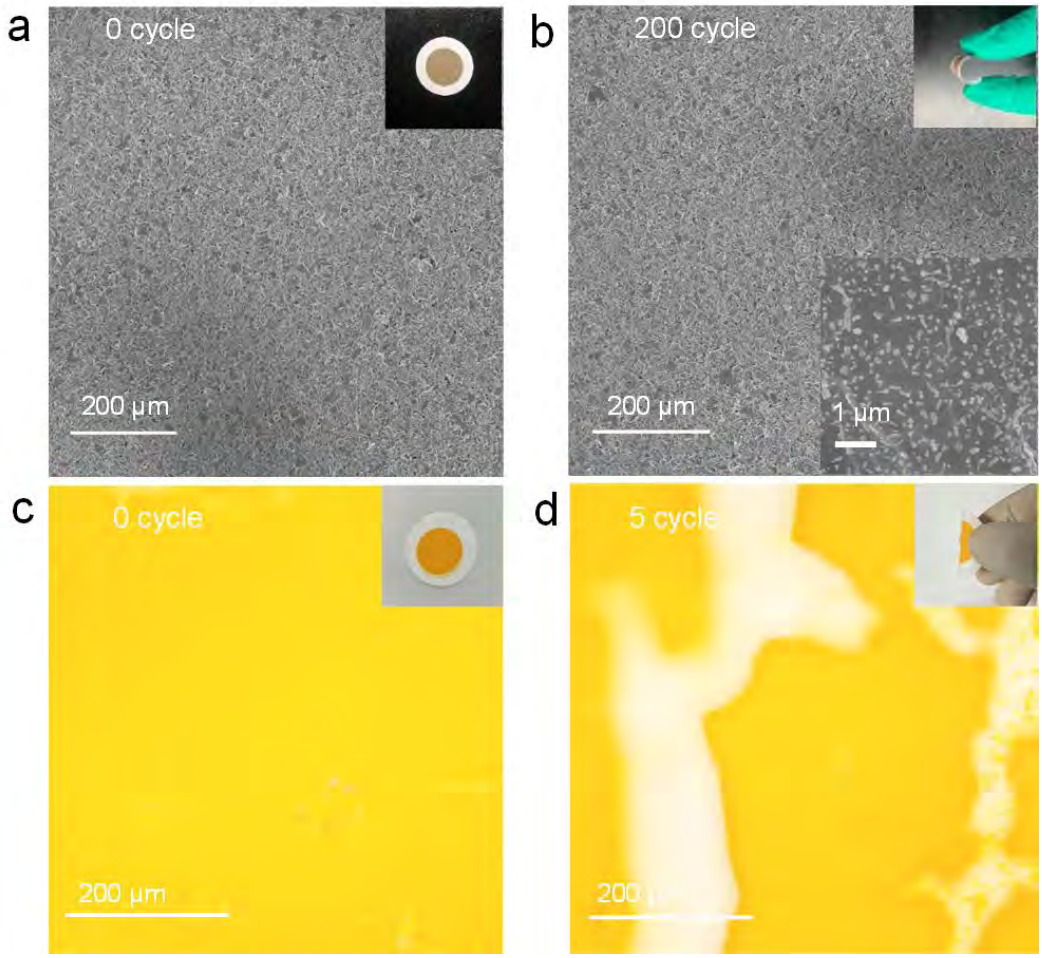

Figure S14. (a) SEM image and picture (inset) of the surface of the pristine BP-2 min Pb-$MAPbBr_3$ film and (b) SEM image after bending 200 times with the inset showing the photograph and close-up SEM image. (c) Optical image and picture (inset) of the surface of the pristine $MAPbBr_3$ film and (d) optical image after bending 5 times with the inset showing the photograph.

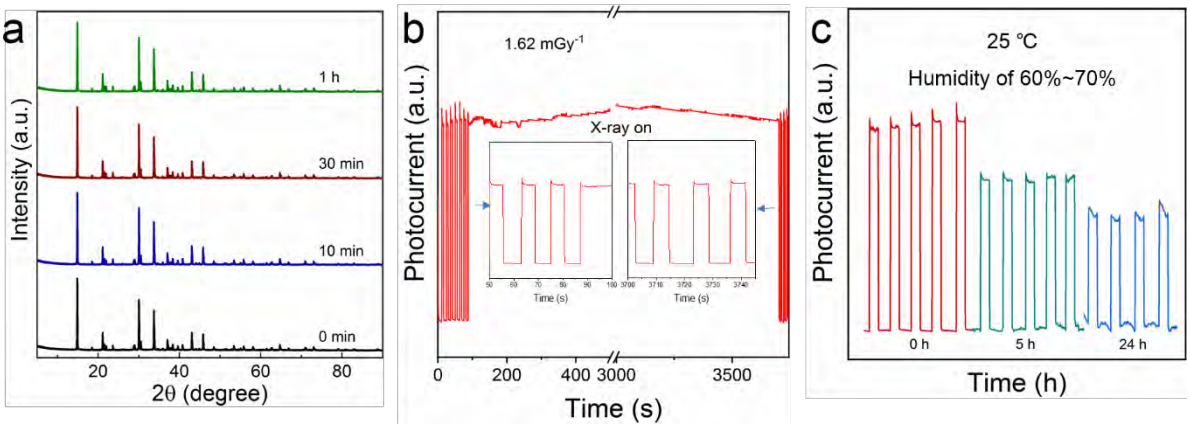

Figure S15. (a) XRD patterns of BP-2 min Pb-$MAPbBr_3$ heterostructure based film under continuous X-ray exposure (1.62 $mGys^{-1}$ dose rate) for 0 s, 600 s, 1200 s and 3600 s. (b) Heterostructure based detector operation stability under a 1.62 $mGys^{-1}$ dose rate for 3600 s. (c) X-ray response stability of heterostructure based detector under storage at 25 ℃ with humidity of 60%~70% for 24h.